J|A|C|S
ARTICLES

Published on Web 11/30/2009

Block Copolymers with a Twist

Rong-Ming Ho,*,† Yeo-Wan Chiang,† Chun-Ku Chen,† Hsin-Wei Wang,†
Hirokazu Hasegawa,*,‡ Satoshi Akasaka,‡ Edwin L. Thomas,§ Christian Burger,*,|| and Benjamin S. Hsiao||

Department of Chemical Engineering, National Tsing Hua University, Hsinchu 30013, Taiwan, Department of Polymer Chemistry, Kyoto University, Kyoto 615-8510, Japan, Department of Materials Science and Engineering, Institute for Soldier Nanotechnologies, Massachusetts Institute of Technology, Cambridge, Massachusetts 02139, and Department of Chemistry, Stony Brook University, Stony Brook, New York 11794-3400

Received October 2, 2009; E-mail: rmho@mx.nthu.edu.tw

Abstract: Chiral block copolymers (BCPs*) comprising chiral entities were designed to fabricate helical architectures (i.e., twisted morphologies) from self-assembly. A new helical phase (H*) with *P*622 symmetry was discovered in the self-assembly of poly(styrene)-*b*-poly(L-lactide) (PS-PLLA) BCPs*. Hexagonally packed, interdigitated PLLA helical microdomains in a PS matrix were directly visualized by electron tomography. The phase diagram of the PS-PLLA BCPs* was also established. Phase transitions from the H* phase to the stable cylinder and gyroid phases were found after long-time annealing, suggesting that the H* is a long-lived metastable phase. In contrast to racemic poly(styrene)-*b*-poly(D,L-lactide) BCPs, chiral interaction significantly enhances the incompatibility between achiral PS and chiral PLLA blocks in the PS-PLLA BCPs* and can be estimated through the determination of the interaction parameter.

Introduction

Self-assembly is the spontaneous organization of components into patterns or structures by cooperating secondary interactions (i.e., noncovalent bonding forces).[1−3] Different length-scale architectures can be formed from the self-assembly of biological molecules and macromolecules by interplay of various secondary interactions. Among biological architectures the helical morphology is perhaps the most fascinating morphology in nature. On a molecular length scale, the formation of single-stranded peptide helices and double-stranded DNA helices by hydrogen bonding is well-known. Aside from the helical chain conformations, helical architectures are also observed in different length scales, such as *Gastrospirillism* (spiral bacteria with a helical pitch length ∼tens of nanometers), *Spirulina* (spiral alga with a helical pitch length ∼tens of micrometers), and the *snail* (spiral shell with a helical pitch length ∼several millimeters to centimeters). The development of the self-assembly of synthetic molecules and macromolecules into helical morphologies has been inspired by nature. Synthetic molecules and macromolecules for constructing helical architectures at different length scales have all been demonstrated.[4−11] Block copolymers (BCPs) are able to self-assemble into 1D, 2D, and 3D periodic nanostructures in bulk because of the incompatibility and the chemical connection between constitutent blocks.[12] Amphiphilic BCPs that contain a charged chiral block have been synthesized.[5] Hierarchical superstructures with a helical sense were obtained by the solution casting of those BCPs, suggesting that the chiral block, aside from amphiphilicity, ionic bonding, and electrostatic effects, plays an important role in the formation of helical nanostructures from solution.

Recently, a diblock copolymer that contains both achiral and chiral blocks, poly(styrene)-*b*-poly(L-lactide) (PS-PLLA), was designed for self-assembly.[13−18] Unique transmission electron microscopy (TEM) projection images comprising twisted mor-

† National Tsing Hua University.
‡ Kyoto University.
§ Massachusetts Institute of Technology.
|| Stony Brook University.

(1) Lehn, J.-M. *Science* **1985**, *227*, 849–856.
(2) Whitesides, G. M.; Mathias, J. P.; Seto, C. T. *Science* **1991**, *254*, 1312–1319.
(3) Lehn, J.-M. *Supramolecular Chemistry*; VCH: Weinheim, 1995; pp 1−4.
(4) Nelson, J. C.; Saven, J. G.; Moore, J. S.; Wolynes, P. G. *Science* **1997**, *277*, 1793–1796.
(5) Cornelissen, J. J. L. M.; Fischer, M.; Sommerdijk, N. A. J. M.; Nolte, R. J. M. *Science* **1998**, *280*, 1427–1430.
(6) Engelkamp, H.; Middelbeek, S.; Nolte, R. J. M. *Science* **1999**, *284*, 785–788.
(7) Orr, G. W.; Barbour, L. J.; Atwood, J. L. *Science* **1999**, *285*, 1049–1052.
(8) Li, C. Y.; Cheng, S. Z. D.; Ge, J. J.; Bai, F.; Zhang, J. Z.; Mann, I. K.; Harris, F. W.; Chien, L.-C.; Yan, D.; He, T.; Lotz, B. *Phys. Rev. Lett.* **1999**, *83*, 4558–4561.
(9) Hulvat, J. F.; Stupp, S. I. *Angew. Chem., Int. Ed.* **2002**, *41*, 1705–1709.
(10) Ungar, G.; Liu, Y.; Zeng, X.; Percec, V.; Cho, W.-D. *Science* **2003**, *299*, 1208–1211.
(11) de Jong, J. J. D.; Lucas, L. N.; Kellogg, R. M.; van Esch, J. H.; Feringa, B. L. *Science* **2004**, *304*, 278–281.
(12) Bates, F. S.; Fredrickson, G. H. *Phys. Today* **1999**, *52*, 32–38.
(13) Ho, R.-M.; Chiang, Y.-W.; Tsai, C.-C.; Lin, C.-C.; Ko, B.-T.; Huang, B.-H. *J. Am. Chem. Soc.* **2004**, *126*, 2704–2705.
(14) Chiang, Y.-W.; Ho, R.-M.; Ko, B.-T.; Lin, C.-C. *Angew. Chem., Int. Ed.* **2005**, *44*, 7969–7972.
(15) Ho, R.-M.; Chen, C.-K.; Chiang, Y.-W. *Adv. Mater.* **2006**, *18*, 2355–2358.
(16) Chiang, Y.-W.; Ho, R.-M.; Thomas, E. L.; Burger, C.; Hsiao, B. S. *Adv. Funct. Mater.* **2009**, *19*, 448–459.
(17) Tseng, W.-H.; Chen, C.-K.; Chiang, Y.-W.; Ho, R.-M. *J. Am. Chem. Soc.* **2009**, *131*, 1356–1357.

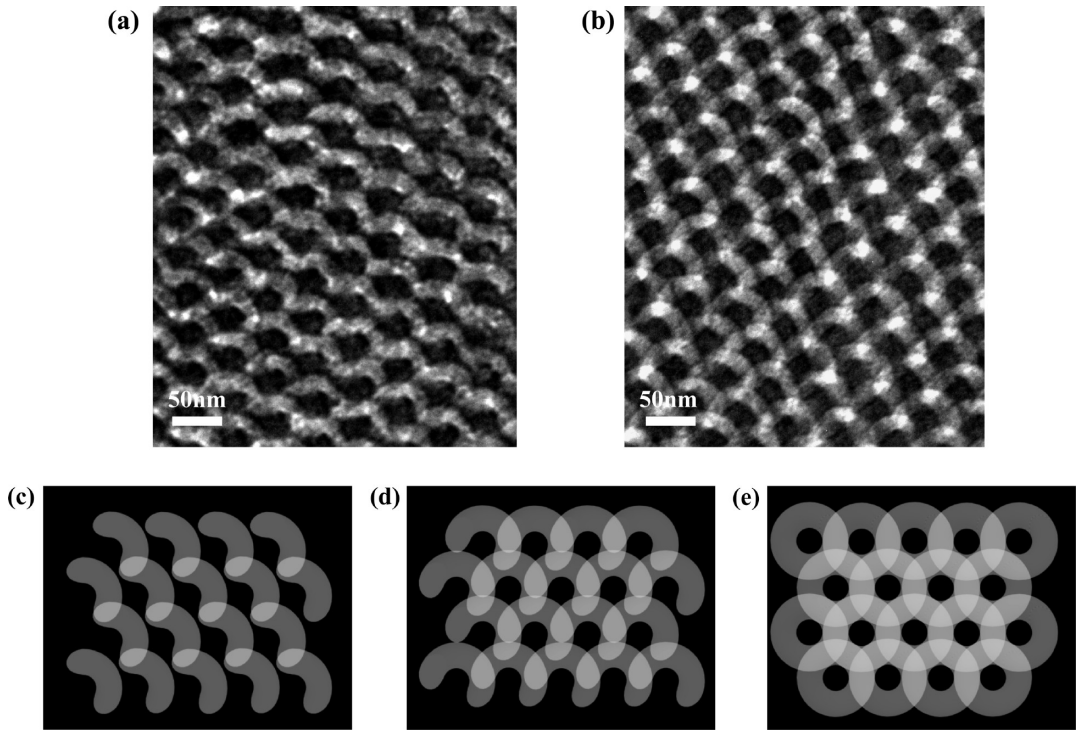

Figure 1. Bright-field TEM micrographs of PS280-PLLA127 ($f_{PLLA}^{v} = 0.34$) viewed parallel to the central axes of the H* phase with (a) 50 nm thick samples, (b) 70 nm thick sample. Simulated top-view projection images with (c) $t < 0.5P$, (d) $t = 0.5P$, and (f) $t \geq P$ where t is sample thickness and P is helical pitch length.

phologies in the self-assembled nanostructure of the PS-PLLA with a volume fraction of PLLA (f_{PLLA}^{v}) = 0.34 prove the presence of a helical phase (H*), whereas no such projection image can be found in racemic BCPs (that is poly(styrene)-*b*-poly(D,L-lactide) (PS-PLA)).[19] For PS-PLLA with $f_{PLLA}^{v} = 0.65$, a core−shell cylinder phase with a helical sense (CS*), in which PS microdomains appear as shells and PLLA microdomains appear as a matrix and cores, could be found.[15] The formation of the H* and CS* phases depends on the contribution of chiral entities. We thus named this block copolymer system as a chiral block copolymer (BCP*). This work aims to thoroughly examine the twisted phase in the self-assembly of the PS-PLLA BCPs*. An H* phase with a *P*622 space group in the self-assembly of diblock copolymers is thus defined for the first time. A phase diagram of the PS-PLLA BCPs* is established to comprehend the chiral effect on the self-assembly of BCPs. Also, the H* phase is identified as a long-lived metastable phase that might transform into stable phases through thermal annealing. Most interestingly, the chiral interaction induced by the intermolecular packing of chiral polymer chains with a helical conformation is evidenced by the stronger segregation strength in the PS-PLLA BCPs* than that in the racemic PS-PLA BCPs.

Results and Discussion

Identification of a New H* Phase. A bulk sample of PS280-PLLA127 (f_{PLLA}^{v} = 0.34), quenched from a microphase-separated, ordered melt at 175 °C, was sectioned using an ultramicrotome for TEM observation. Complicated projection images that show twisted morphologies are obtained in which dispersed PLLA microdomains appear bright and the PS matrix appears dark because of RuO_4 staining (Figure 1). Notably, those twisted morphologies are highly sensitive to the tilting and the sample thickness under TEM observation (Figures S1 and S2 of the Supporting Information) because of the imaging mechanism by which 2D TEM projection represents a 3D object. Samples of various thicknesses were utilized to further examine the complicated projection images of the microphase-separated phase. As presented in part a of Figure 1, a helixlike morphology was observed in a typical 50 nm thick sample. Additionally, the projection image exhibits a crescentlike morphology, the arcs of which depend on the sample thickness in the projection. Therefore, a semicircular morphology is obtained in the 70 nm thick sample (part b of Figure 1). To extract all possible information from these unusual projections, simulations of the projections of the helical phase with a specific pitch length (P) (especially for projection images viewed along the central axes of the helices, that is, a top-view projection) were thus conducted by assuming that the sample has a specific thickness (t) (parts c−e of Figure 1). According to the simulated results, the formed crescentlike projection image (part c of Figure 1) gradually extends with an increase of t and forms a semicircular (i.e., half-turn helical) morphology when $t = 0.5P$ (part d of Figure 1). Finally, a full-turn helical projection image (i.e., donut-shaped morphology) is observed when $t \geq P$ (part e of Figure 1). As shown in part a of Figure 1, the TEM projection image is identical to the simulated top-view projection image of $t < 0.5P$ (part c of Figure 1), showing a helical projection image with an incomplete pitch length. This indicates that the helixlike morphology of the 50 nm thick sample is attributed to connections among the crescentlike microdomains. Therefore, on the basis of the assumed geometry, a donut-shaped morphology is expected from the projection of a full-turn helix when $t \geq P$ (part e of Figure 1). Part a of Figure 2 presents a TEM micrograph of a 150 nm thick sample. Consistent with the

(18) Ho, R.-M.; Chen, C.-K.; Chiang, Y.-W. *Macromol. Rapid Commun.* **2009**, *30*, 1439–1456.
(19) Zalusky, A. S.; Olayo-Valles, R.; Wolf, J. H.; Hillmyer, M. A. *J. Am. Chem. Soc.* **2002**, *124*, 12761–12773.

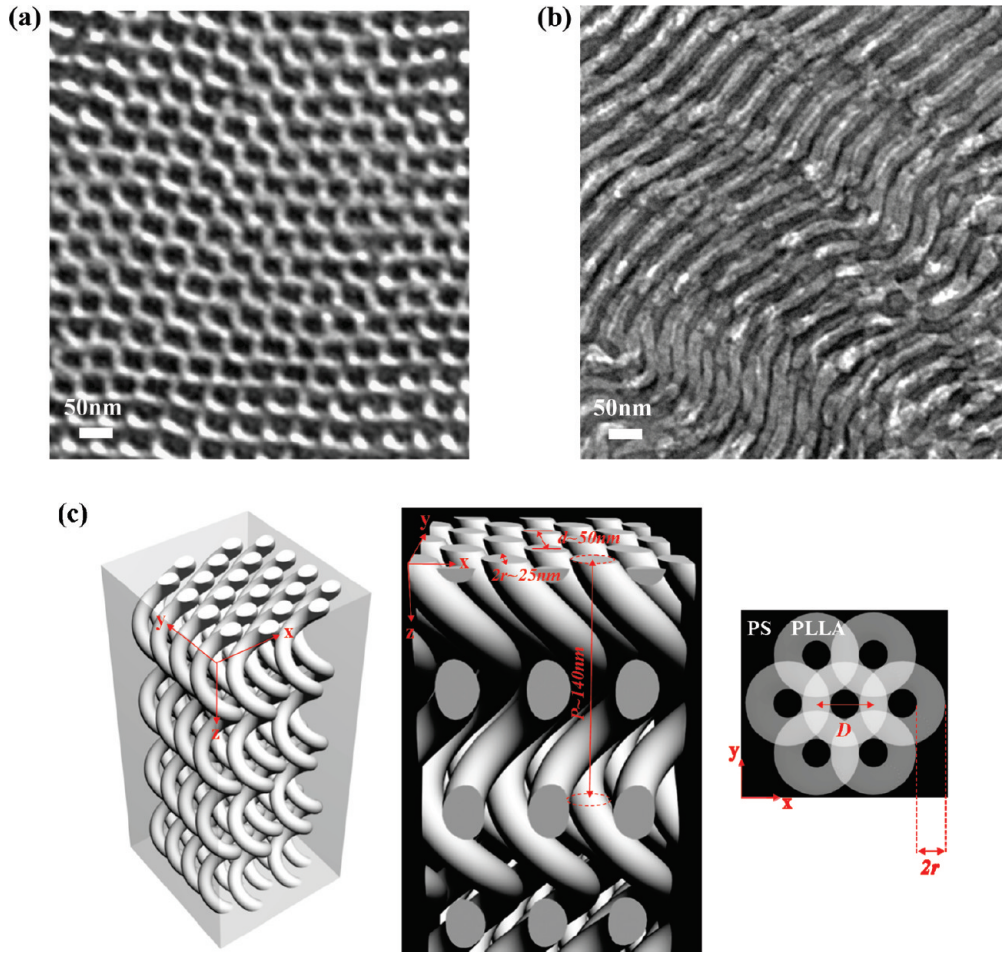

Figure 2. Bright-field TEM micrographs of PS280-PLLA127 ($f_{PLLA}^{v} = 0.34$) viewed (a) parallel, and (b) normal to the helical central axes (the z direction) of the H* phase. (c) Schematic H* phase in which the helical microdomains are packed in a hexagonal lattice with an interdigitated character (left), prospective view (center), and simulated image projected along the z direction of the H* phase (right).

simulated result, a donut-shaped morphology with a hexagonal symmetry can be clearly identified, indicating that the projection image is generated by hexagonally packed PLLA helical microdomains in a PS matrix. A wavelike morphology can also be observed, consistent with the expected helical projection image viewed normal to the central axis of the helical phase (i.e., a side-view projection) (part b of Figure 2). Consequently, given the known parameters, the intrinsic pitch length of the helix can be determined from the volume fraction of the PLLA blocks. The volume fraction of the suggested helical phase can be described by the following equations.

$$f_{PLLA}^{v} = C\sqrt{(\pi D/P)^2 + 1} \quad (1)$$

$$C = (\sqrt{3}\pi r^2)/(2d^2) \quad (2)$$

P is the helical pitch length, D is the projected diameter of the helix along the central axis (~50 nm determined by TEM), r is the radius of the helical microdomain (~12.5 nm determined by TEM and FESEM), and d is the interspacing of helices (~50.0 nm determined by SAXS). From the volume fraction of PS280-PLLA127 ($f_{PLLA}^{v} = 0.34$), the helical pitch length is calculated as 140 nm, consistent with the result estimated by experiments and simulations. Consequently, we suggest that a twisted morphology, the H* phase, appears as hexagonally packed, interdigitated helical microdomains as shown in part c of Figure 2.

Recently, a new method, TEM tomography, for imaging the morphologies and especially nanoscale features of soft materials[20−22] in 3D space, has been developed. A direct imaging of a 3D nanoscale object is constructed from a series of tilted projections. By taking advantage of the degradable character of polylactide, the self-assembled H* phase after hydrolysis can be utilized to prepare a PS template with helical nanochannels (mesoporous helical materials). The sol−gel reaction forming silicate microdomains is then conducted within this PS template to fabricate helical nanocomposites.[17] Accordingly, in contrast to the inaccessibility of the image reconstruction in RuO_4-stained PS-PLLA samples, the PS/SiO_2 nanocomposites can be directly visualized by TEM without RuO_4 staining because of a significant increase in the mass−thickness contrast of the SiO_2 helices (Figure S3 of the Supporting Information). As shown in parts a and b of Figure 3, similar to the projection images of the H* phase but with inverted mass−thickness contrast, semicircular and donut-shaped projection images of 70 nm and 150 nm thick samples are obtained, respectively. Furthermore, 6-fold darkest spots can be clearly identified because of the overlapping parts of the hexagonally packed, interdigitated helical microdomains with significant contrast along the helical

(20) Frank, J. *Electron Tomography*; Springer-Verlag: New York, 2006.
(21) Yamauchi, K.; Takahashi, K.; Hasegawa, H.; Iatrou, H.; Hadjichristidis, N.; Kaneko, T.; Nishikawa, Y.; Jinnai, H.; Matsui, T.; Nishioka, H.; Shimizu, M.; Fukukawa, H. *Macromolecules* **2003**, *36*, 6962–6966.
(22) Bartus, J.; Weng, D.; Vogl, O. *Polym. Int.* **1994**, *34*, 433–442.

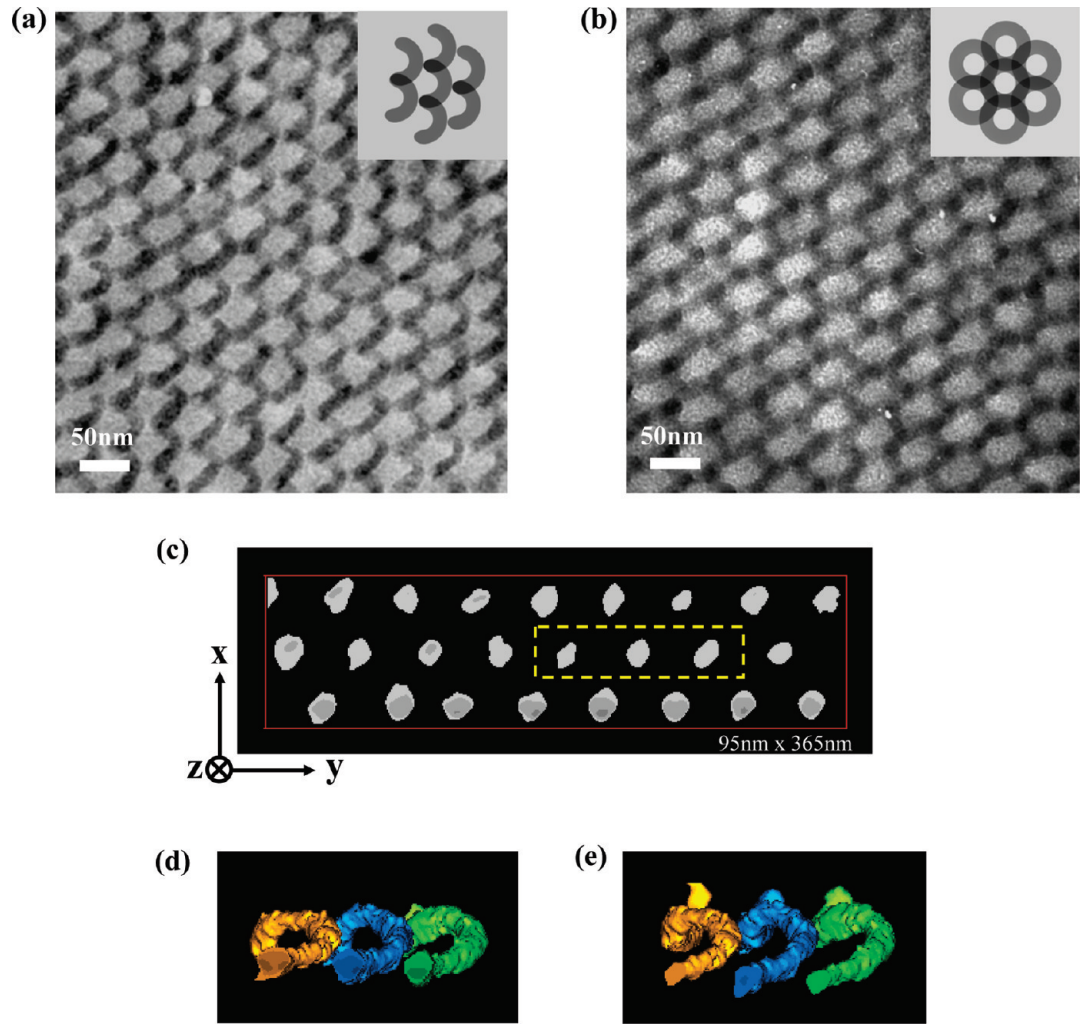

Figure 3. Bright-field TEM micrographs of PS/SiO_2 helical nanocomposites viewed parallel to the helical central axes for (a) 70 nm thick, and (b) 150 nm thick samples. Insets represent the corresponding simulated projection images. 3D TEM visualization with a dark matrix: (c) cross-sectional view after binarization, and (d) and (e) images viewed parallel to the helical central axes and slightly tilted from the helical central axes after binarization and segmentation, respectively (the domain within the box with the dashed perimeter in (c)).

central axes. Therefore, this PS/SiO_2 helical nanocomposites can provide a perfect sample with appropriate contrast for the image reconstruction of 3D tomography (part b of Figure 3). Parts c−e of Figure 3 present a 3D visualization of the SiO_2 helices using a cross-sectional slice. Hexagonally packed SiO_2 helices can be observed by direct 3D visualization, confirming the hexagonal-cylinder-like character inferred from the scattering results (part c of Figure 3).[17] Also, well-defined SiO_2 helices with a regular pitch length and an interdigitated character can be clearly recognized in the PS/SiO_2 helical nanocomposites (parts d and e of Figure 3). According to the 3D TEM results, the pitch length is approximately 140 nm, consistent with the result calculated from eq 1. As a result, the H* phase possessing hexagonally packed, interdigitated PLLA helical microdomains in a PS matrix is thus identified. Furthermore, the self-assembled H* phase from PS-PLLA BCPs* all appeared as left-handed helical microdomains. As described, the formation of the H* phase is attributed to the contribution of chiral configuration. The development of the H* phase from the self-assembly of BCPs* gives rise to important questions such as "Is it possible to transfer chiral information from molecular level to the macroscopic level?" and "Is it possible to control the handedness of the H* phase?". In nature, homochiral evolution is a key molecular process for communication, replication, and enzyme catalysis through the association of molecular and supramolecular chirality. It is essential to understand the results of chiral information transfer and their corresponding mechanisms. It is intuitive to expect one-handed character from chiral information transfer through homochiral evolution. Nevertheless, how the intermolecular packing at the interface and molecular chirality determines the handedness of the H* phase is still an open question. Systematic studies about the handedness control of self-assembled morphologies are necessary to gain in-depth understanding of the behavior and corresponding mechanisms. The relevant work is still in progress.

The space group of the hexagonally packed cylinders is identified as *P6mm* because of the 6-fold symmetry and the mirror images on the hexagonal lattice plane in 2D. In contrast to the symmetry of the cylinder, the helical texture cannot be superimposed on its mirror image. As a result, *P*6 and *P*622 are two possible symmetries for the hexagonally packed helical microdomains. Contrary to the *P*6 space group, *P*622 has a screw axis that is normal to the long axis of the hexagonal lattice on the hexagonal lattice plane for a helical object. Because of its higher symmetry for the hexagonally packed helical microdomains, the H* phase is thus identified as *P*622.

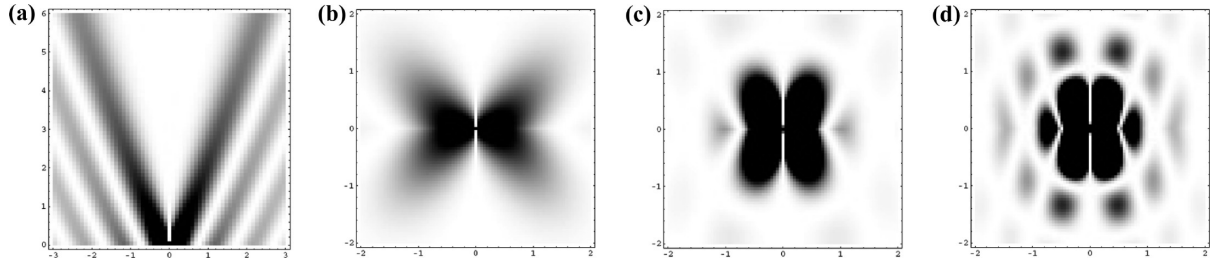

Figure 4. Calculated form factors for a single winding of a helix normal to the helical central axis with different diameters of the helical microdomain: (a) helix wire ($R = 0$); (b) helix with $R = 0.5\ D$; (c) $R = D$; (d) $R = 1.5\ D$. Horizontal axis is Ds_{12}; vertical axis is Ps_3. Replicating the single winding to a continuous helix concentrates the scattering intensity on the $Ps_3 = l$(integer) layer lines.

A quantitative model is proposed to investigate the H* phase by scattering. The form factor (F) of a helix can be factorized as

$$F(s_{12},\phi,s_3) = F_{\text{helix}}(D,s_{12},\phi,s_3)F_{\text{flesh}}(R,s)F_{\text{interf}}(t,s) \qquad (3)$$

where (s_{12},ϕ,s_3) are the components of the scattering vector $\vec{s}$ in cylindrical coordinates and $s = |\vec{s}| = 2\lambda^{-1}\sin\theta$, λ is the wavelength, and 2θ is the scattering angle.

F_{helix}, F_{flesh}, and F_{interf} are described as follows.

$$F_{\text{helix}}(D,s_{12},\phi,s_3) = \sum_{l=-\infty}^{\infty} J_l(\pi D s_{12})\exp(il\phi)\delta(s_3 - l/P) \qquad (4)$$

$$F_{\text{flesh}}(R,s) = 2J_1(\pi Rs)/(\pi Rs) \qquad (5)$$

$$F_{\text{interf}}(t,s) = \exp(-\pi t^2 s^2) \qquad (6)$$

F_{helix} is the 3D Fourier transform of the helix skeleton described as a winding Dirac δ-function. F_{flesh} is the 3D Fourier transform of a 3D isotropic function, which upon convolution with a δ-skeleton approximately yields the thickness of the helix with a circular cross section. F_{interf} is the 3D Fourier transform of a 3D isotropic function, which upon convolution with a 3D Heaviside density step leads to a smooth sigmoidal density transition. J_n is the Bessel function of the first kind of order n, P is the pitch length; $l = Ps_3$ (integer), D is the projected diameter of the helix along the central axis, R is the diameter of a helical microdomain ($R = 2r$), and t is a finite density transition of width between the helical microdomain and the matrix. Part a of Figure 4 shows the calculated form factor of a helix normal to the helical central axis for $R = 0$ and $P = D$ in which the X-shaped pattern can be clearly observed, indicating the disappearance of all (00l) and some mixed (hkl) reflections. In contrast, as the thickness of the helical microdomains is considered ($R \neq 0$) in the pattern of the form factor (eq 5), and the X-shaped pattern becomes more and more ambiguous when the thickness of the helical microdomains increases (parts b−d of Figure 4). As a result, all of the mixed (hkl) reflections could be feasibly suppressed by the form factor of the helix with an increase of the diameter of the helical microdomains. Accordingly, only the ($hk0$) reflections can be observed so that simple hexagonal reflections are thus obtained in the scattering pattern of the H* phase because of the hexagonal symmetry (Figure S4 of the Supporting Information).

Phase Behavior of BCP*. To truly acquire the H* phase, systematic studies on the phase diagram of PS-PLLA BCPs* is essential. A series of PS-PLLA BCPs* with different compositions (i.e., various volume fractions of PLLA blocks) were synthesized to establish the BCP* phase diagram. The corresponding phase identifications are listed in Table S1 of the Supporting Information. Similar to the self-assembled morphologies of the racemic PS-PLA BCPs, those microphase-separated morphologies exhibit typical phases as predicted by the theory of BCP thermodynamics. By contrast, helical morphologies are observed with $f_{\text{PLLA}}{}^{v} = 0.32-0.36$ in the PS-PLLA BCPs*, whereas no such a morphology can be found in the racemic PS-PLA BCPs. Also, the formation of the H* phase depends not only on the composition of the PS-PLLA BCPs* but also on their corresponding molecular weight. Instead of an H* phase, a typical gyroid phase (G) is obtained in low-molecular-weight PS-PLLA BCPs* with $f_{\text{PLLA}}{}^{v} = 0.35$. A wagon-wheel morphology with 3-fold symmetry (part a of Figure 5), corresponding to the [111] projection of the G phase, and a morphology with 4-fold symmetry (part b of Figure 5), corresponding to the [100] projection of the G phase, are observed.[23] Corresponding SAXS results consisting of the reflections at a q^* ratio of $\sqrt{3}$ and $\sqrt{4}$ further verify the identification of the G phase (part c of Figure 5). Consequently, a phase diagram of the PS-rich PS-PLLA BCPs* with the molecular-weight and composition dependence is proposed (part d of Figure 5).

Thermally induced phase transitions between equilibrium morphologies in BCP self-assembly are well-known such as the lamellae (L) to G and the G to hexagonally packed cylinders (HC) transitions by varying the value of the Flory−Huggins parameter χ scaling with temperature as $1/T$ at essentially constant BCP composition.[24−28] Also, a metastable perforated layered (PL) phase[29−32] can be transformed into stable phases such as the G and HC phases through thermal annealing,[24−27,33,34] revealing that the metastability of these self-assembled phases is promising in the morphological manipulation. Like the

(23) Hajdu k, D. A.; Harper, P. E.; Gruner, S. M.; Honeker, C. C.; Kim, G.; Thomas, E. L.; Fetters, L. J. *Macromolecules* **1994**, *27*, 4063–4075.
(24) Forster, S.; Khandpur, A. K.; Zhao, J.; Bates, F. S.; Hamley, I. W.; Ryan, A. J. *Macromolecules* **1994**, *27*, 6922–6935.
(25) Khandpur, A. K.; Forster, S.; Bates, F. S.; Hamley, I. W.; Ryan, A. J.; Bras, W.; Almdal, K.; Mortensen, K. *Macromolecules* **1995**, *28*, 8796–8806.
(26) Hillmyer, M. A.; Bates, F. S.; Almdal, K.; Mortensen, K.; Ryan, A. J.; Fairclough, J. P. A. *Science* **1996**, *271*, 976–978.
(27) Hillmyer, M. A.; Bates, F. S. *Macromolecules* **1996**, *29*, 6994–7002.
(28) Hajduk, D. A.; Ho, R.-M.; Hillmyer, M. A.; Bates, F. S.; Almdal, K. *J. Phys. Chem. B* **1998**, *102*, 1356–1363.
(29) Matsen, M. W.; Bates, F. S. *Macromolecules* **1996**, *29*, 1091–1098.
(30) Matsen, M. W.; Bates, F. S. *Macromolecules* **1996**, *29*, 7641–7644.
(31) Fredrickson, G. H. *Macromolecules* **1991**, *24*, 3456–3458.
(32) Hamley, I. W.; Bates, F. S. *J. Chem. Phys.* **1994**, *100*, 6813–6817.
(33) Schulz, M. F.; Khandpur, A. K.; Bates, F. S.; Almdal, K.; Mortensen, K.; Hajduk, D. A.; Gruner, S. M. *Macromolecules* **1996**, *29*, 2857–2867.
(34) Hajduk, D. A.; Takenouchi, H.; Hillmyer, M. A.; Bates, F. S.; Vigild, M. E.; Almdal, K. *Macromolecules* **1997**, *30*, 3788–3795.

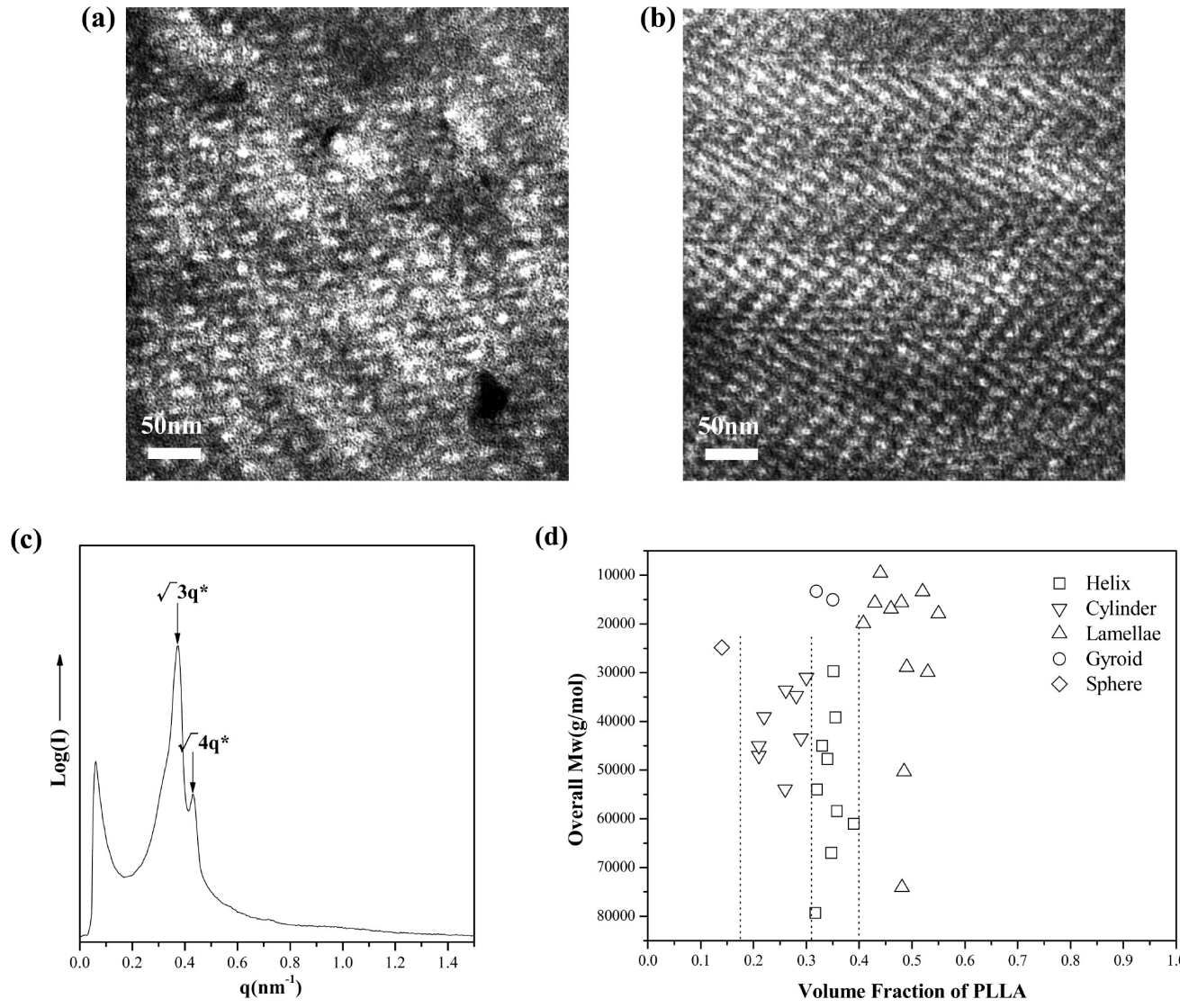

Figure 5. Bright-field TEM micrographs of the gyroid phase in the low-molecular-weight PS83-PLLA41 ($f_{PLLA}^{v} = 0.35$), viewed along (a) [111] and (b) [100] directions. (c) 1D SAXS profile extracted from the 2D diffraction pattern by azimuthally averaging scattered intensity over the whole range of angles. (d) Phase diagram of the PS-PLLA BCPs* with respect to overal molecular weight and composition.

transitions in the PL phase, the H* phase exhibits interesting morphological transitions. After long-time annealing (for more than 1 week), a stable HC morphology can be found in PS280-PLLA127 ($f_{PLLA}^{v} = 0.34$) sample (part a of Figure 6) evidenced by 1D SAXS reflections at the q^* ratios of $1:\sqrt{4}:\sqrt{7}:\sqrt{9}$ (part b of Figure 6). Additionally, the phase transition reveals that the transition kinetics strongly depends on the composition. Subsequent extended annealing of PS327-PLLA188 ($f_{PLLA}^{v} = 0.39$), consisting of the H* phase at the preset temperature, for a long time induces a transition to the G phase (part c of Figure 6) evidenced by 1D SAXS reflections at a q^* ratio of $\sqrt{3}:\sqrt{4}$ (part d of Figure 6). Nonequilibrium phases such as the PL phase formed as a consequence of sample preparation or a phase-transition mechanism are easily misinterpreted as stable phases. The most reliable method is to demonstrate the reversibility of the transitions between ordered morphologies. A nonequilibrium phase transition is in principle an irreversible process, whereas transitions between equilibrium states should be thermally reversible. For instance, the PL is a metastable phase and is able to transfer into stable G phase, whereas the reverse transition from G to PL does not take place. Similarly, in the phase transitions of H* to HC and H* to G, no further transitions were observed upon continued isothermal annealing after the formation of the HC or G phase. Moreover, an attempt to recover the H* morphology by cooling the G or HC phases to lower temperatures was unsuccessful. The BCP* phase diagram also demonstrates a dependence of the formation of the H* phase on the molecular weight as the H* phase is apparently present in the high-molecular-weight region (part d of Figure 5). We thus suggest that the formation of the H* phase is attributed to the slow kinetics associated with long, highly entangled chains. Accordingly, the observation of the metastable H* phase derives from a kinetically trapped process because of the prolonged relaxation time. Consequently, the H* phase is regarded as a long-lived metastable state.

Effect of Chiral Interaction. Remarkable discrepancies between the phase boundary of the racemic PS-PLA BCPs and chiral PS-PLLA BCP*s were found; in particular, a variation in the boundary of the order−disorder transition (ODT) is identified. Here, the ODT temperature (T_{ODT}) values were determined through temperature-resolved SAXS experiments. As illustrated, parts a and b of Figure 7 show the SAXS profiles

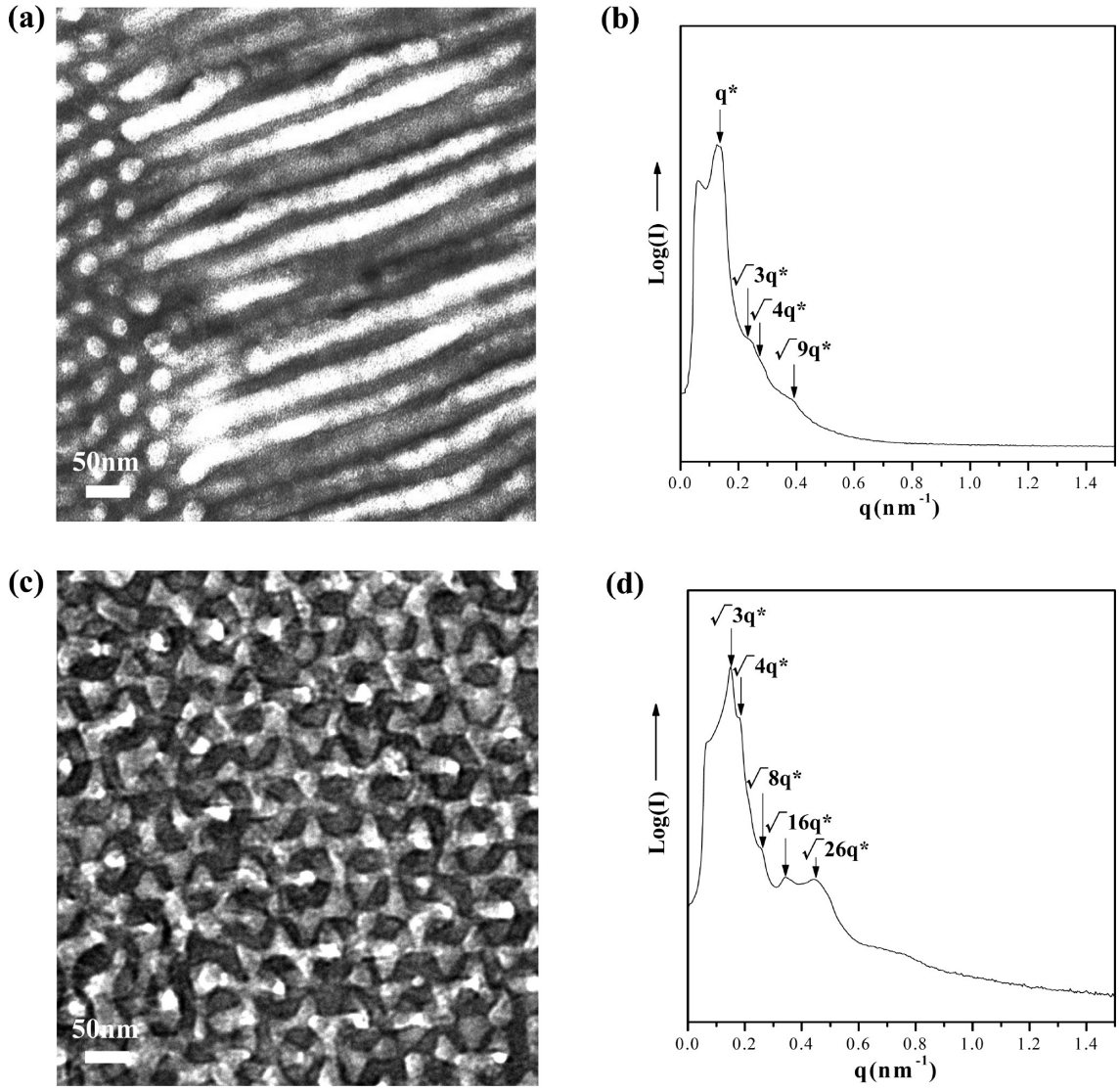

Figure 6. Bright-field TEM micrographs of (a) HC phase in PS280-PLLA127 ($f_{PLLA}{}^{v} = 0.34$) and (c) G phase in PS327-PLLA188 ($f_{PLLA}{}^{v} = 0.39$) after long-time annealing at 140 °C. (b) and (d) are the corresponding 1D SAXS profiles of (a) and (c), respectively.

of PS47-PLLA32 ($f_{PLLA}{}^{v} = 0.44$) taken at various temperatures during the heating and cooling processes, respectively. A sharp and remarkable change on the SAXS profiles can be clearly discerned at temperatures between 180 and 190 °C. To characterize the change in the SAXS profiles across the ODT, $I_m{}^{-1}$ and $\sigma_q{}^2$ are plotted as a function of reciprocal absolute temperature T^{-1} (parts c and d of Figure 7) where $I_m{}^{-1}$ and $\sigma_q{}^2$ denote the reciprocal of peak intensity and the square of width at the half-maximum intensity of primary scattering peak, respectively. As expected, both $I_m{}^{-1}$ and $\sigma_q{}^2$ curves show a sharp discontinuous change in the temperature range between 180 and 190 °C. Accordingly, the ODT temperature for PS47-PLLA32 ($f_{PLLA}{}^{v} = 0.44$) was thus determined as $T_{ODT} = 180$ °C based on either the results from heating or cooling experiments. Consequently, the T_{ODT} values for a variety of PS-PLLA BCP* samples with lamellar phases were thus determined from temperature-resolved SAXS experiments (part a of Figure 8). In contrast to the T_{ODT} values of the racemic PS-PLA BCPs[19] determined by Hillmyer et al., the T_{ODT} values of the PS-PLLA BCPs* always exceed those of the PS-PLA BCPs for a sample with the equivalent molecular weight and composition, indicating that the segregation strength between the PS and chiral PLLA molecules is higher than that between the PS and racemic PLA molecules.

To comprehend the chiral effect on the BCP* segregation strength, the Flory−Huggins parameter (χ), a critical factor that specifies the interaction strength between different molecules, was determined. The temperature dependence of the χ value is typically described by eq 7:

$$\chi(T) = \alpha/T + \beta \tag{7}$$

where α and β are constants associated with the two types of monomers present in the BCP.

From the known N (overall degree of polymerization) and predicted $(\chi N)_{ODT}$, the temperature dependence of the χ value can be determined by plotting χ as a function of T_{ODT}. Here a typically predicted value $(\chi N)_{ODT}$, 10.5, was adopted in the determination of the χ value of the PS-PLLA BCPs*, which was then compared with that of the racemic PS-PLA BCPs. These χ values extracted from specific temperatures were employed to determine the temperature dependence of the χ value, which is plotted in part b of Figure 8 and described by eq 8.

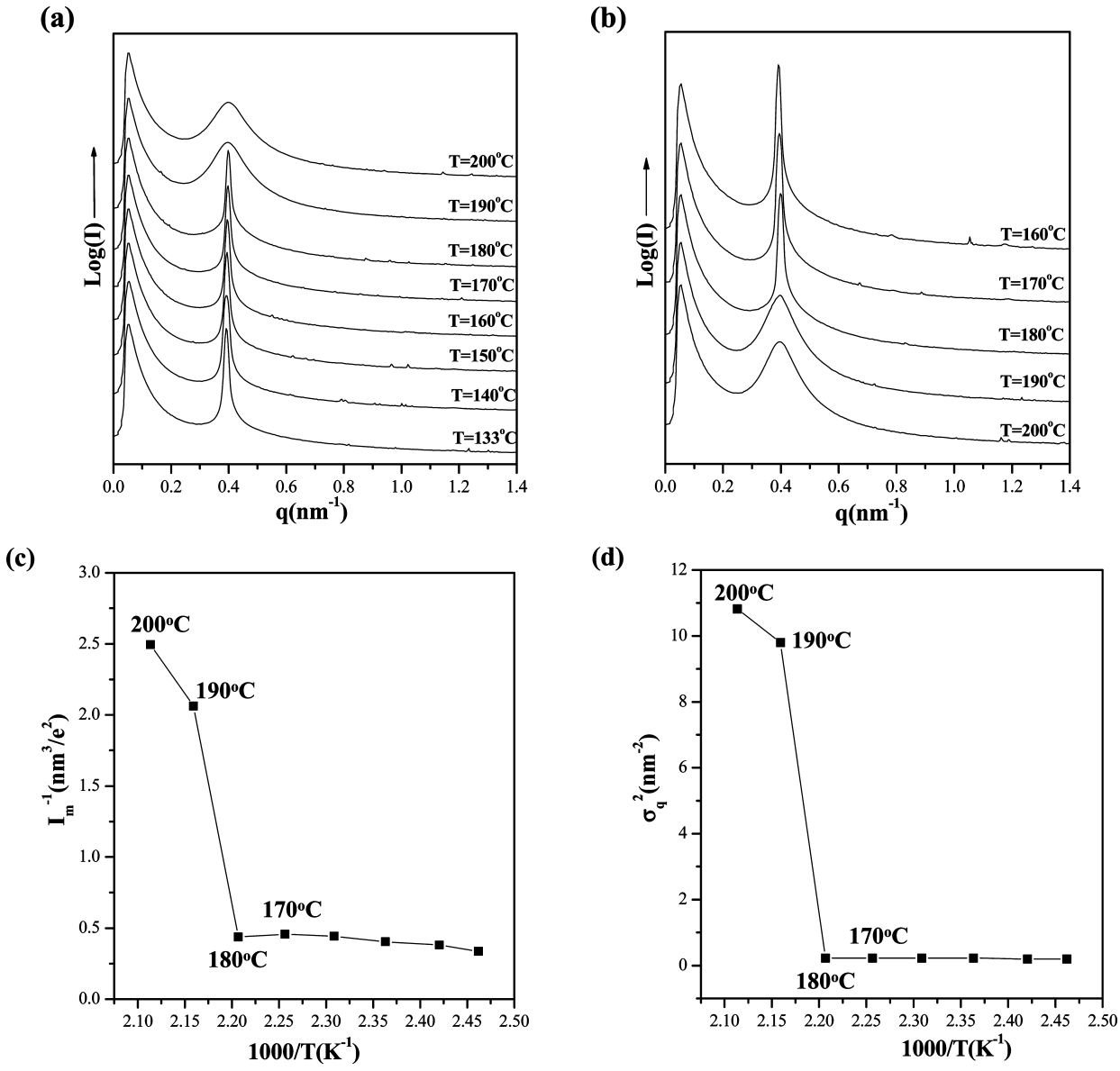

Figure 7. 1D SAXS profiles of PS47-PLLA32 ($f_{PLLA}{}^{v} = 0.44$) taken at various temperatures on (a) heating and (b) cooling processes. An abrupt change on the profile is regarded as a sign of ODT. Plots of (c) $I_m{}^{-1}$ versus T^{-1} and (d) $\sigma_q{}^2$ versus T^{-1} from (a).

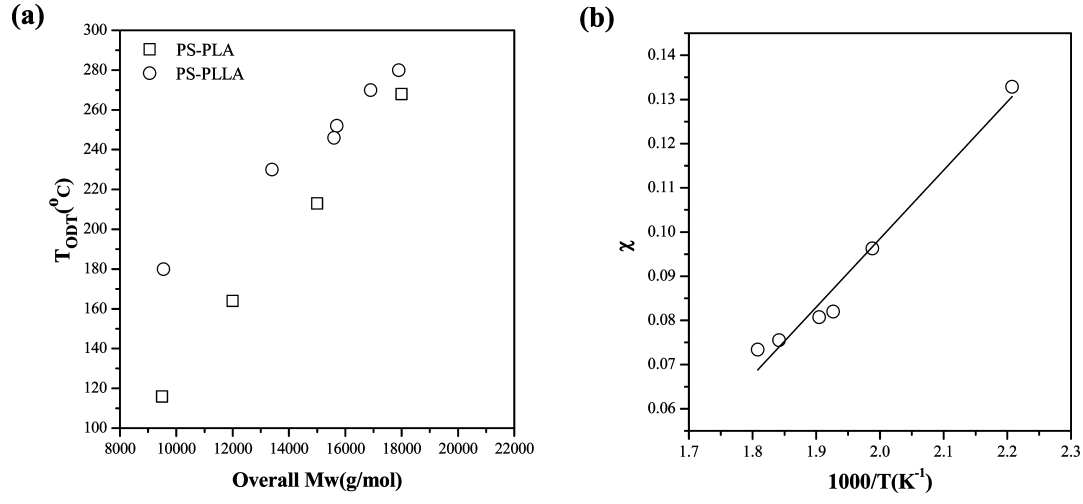

Figure 8. (a) Dependence of T_{ODT} on overall molecular weight for the lamellar phase in PS-PLLA BCPs* and PS-PLA BCPs. The T_{ODT} values of PS-PLA BCPs are adopted from the results of Hillmyer et al.[19] (b) Temperature dependence of χ extracted from the T_{ODT} values.

$$\chi(T) = 154.9/T - 0.211 \quad (8)$$

Notably, the determination of the χ value is based on the predicted $(\chi N)_{ODT} = 10.5$ for a symmetric coil−coil diblock copolymer. However, as the molecular rigidity increases, $(\chi N)_{ODT}$ decreases.[35] Although the rigidity of the chiral PLLA chain exceeds that of the racemic PLA chain (as the characteristic ratios C_∞s of the PLLA and PLA chains are 11.8 and 9.5, respectively),[36] the PS-PLLA BCPs* and the PS-PLA BCPs are suggested to have a slightly lower $(\chi N)_{ODT}$ value, indicating an insignificant change of the $(\chi N)_{ODT}$ value for both the PS-PLLA BCPs* and PS-PLA BCPs. Accordingly, the predicted $(\chi N)_{ODT} = 10.5$ is still pertinent for the estimation of the χ values and the variation in the estimated χ value is still in the reasonable range. The χ values of the chiral PS-PLLA BCPs* and the racemic PS-PLA BCPs at a constant temperature were determined for comparison. As calculated, the χ values of the PS-PLLA BCPs* and racemic PS-PLA BCPs were estimated to be 0.19 from eq 8 and 0.14 from eq 2[19] at 110 °C respectively indicating the higher χ value of the PS-PLLA BCPs* than that of the PS-PLA BCPs. Namely, the incompatibility between PS and chiral PLLA blocks is higher than that between PS and racemic PLA blocks.

The χ value of an AB diblock copolymer strongly depends on the discrepancy between the square root of the cohesive energies of A (E_A) and of B (E_B) (i.e., $\chi \propto (\sqrt{E_A} - \sqrt{E_B})^2$); the variation is related to the packing energies of the A and B chains in the microphase-separated domains. Assuming an AB diblock copolymer in which the E_A is larger than E_B, as the packing energy of A decreases (i.e., the E_A increases), the χ value increases because of an increase of $(\sqrt{E_A} - \sqrt{E_B})$, indicating that the repulsive force (incompatibility) between A and B chains intensifies. According to the solubility parameters (i.e., the square root of the cohesive energies) of the PLLA (22.2 $MPa^{0.5}$) and PS (18.8 $MPa^{0.5}$), the cohesive energy of the PLLA is higher than the PS (that is $(E_{PLLA} - E_{PS}) > 0$). Furthermore, the packing energy of the polymer chains strongly depends on the chain conformation, which is related to its persistence length. As the persistence length of a constituted polymer chain increases, the packing energy decreases. As calculated, the persistence length of the chiral PLLA chain (11.9 angstroms) is larger than that of the racemic PLA chain (10.6 angstroms).[36,37] The estimation of the persistence length is based on the characteristic ratio of the polymer. As reported, the characteristic ratios for poly(lactide)s strongly depend on the D/L-lactide ratio and increase with the tacticity of the polymer from 9.5 for racemic PLA (the D/L-lactide ratio ∼1) to an estimated 11.8 for chiral PLLA (the D/L-lactide ratio = 0).[36] With the known characteristic ratios of the chrial PLLA and racemic PLA chains, the persistence lengths can thus be estimated based on C_6 repeat unit.

The larger persistence length for the chiral PLLA chain is attributed to the formation of a helical chain conformation for a chiral polymer chain,[38] as evidenced by the measurement of circular dichroism (CD). As a result, the longer persistence length of the PLLA helical chain conformation than the racemic polymer is responsible for its lower packing energy, which results in a larger E_{PLLA} (that is $(\sqrt{E_{PLLA}} - \sqrt{E_{PS}}) > (\sqrt{E_{PLA}} - \sqrt{E_{PS}})$) and thus a higher χ parameter of the PS-PLLA BCPs* than the racemic PS-PLLA BCPs. This result is in line with the result of an atomistic molecular dynamics simulation in which the total packing energy of the PS-PLLA BCP* chains is indeed lower than that of the PS-PLA BCP chains (Figure S5 of the Supporting Information).

We thus speculate that the chiral effect not only gives rise to the formation of helical chains (intramolecular effect) but also induces the formation of partially ordered microdomain (intermolecular interaction). The driving force of the formation of the partially ordered microdomain is attributed to the mutual interaction of chiral polymer chains with a helical conformation. This driving force (namely, the intermolecular interaction of chiral polymer chains) is regarded as chiral interaction. The chiral PLLA chain with helical conformation and long persistence length would provide a specific geometrical property (i.e., helical steric hindrance) for self-assembly. In the self-assembly of BCPs, the incompatibility between chemically connected PLLA and PS blocks gives rise to a strongly repulsive force, which reinforces the stretching of the polymer chains and stabilize the helical conformation. Additionally, the chemical linkages of BCP chains are forced to be oriented well at the microphase-separated interface to form a sharp interface for ordering. These oriented chemical linkages of the BCP chains can be regarded as fixed block ends at the microphase-separated interface and may reinforce and amplify the steric effect of the packing during microphase separation (especially when the chain conformation exhibits steric hindrance, as the helical chain conformation). It is similar to the transferred mechanism from molecular chirality to supramolecular chirality in the self-assembly of chiral lipid bilayer molecules.[39,40] The chiral effect is considered as the main ingredient for the formation of helical morphologies. We speculate that the PS-PLLA BCP* chains appear as a bilayer-like nanostructure from self-assembly. On the basis of energetic consideration, the helical steric hindrance gives rise to the twisting and shifting of the bilayer-like nanostructure so as to create the helical curvature at the interface. Furthermore, the chiral effect is enhanced by the introduction of the incompatible PS block that intensifies the helical steric hindrance effect so as to promote the formation of helical microdomains. As a result, twisting and shifting at the microphase-separated interface is initiated by the helical steric hindrance and amplified by the incompatible PS block and the further organization of partially ordered microdomains due to chiral interaction so as to develop helical microdomains. Obviously, the formation of the helical curvature in the H* phase causes an increase of the interfacial area between PS and PLLA microdomains (i.e., increasing the enthalpic penalty associated with incompatibility). However, the enthalpic penalty is balanced by the formation of a partially ordered state in the PLLA microdomains to reach a lower Gibbs free energy state.

Conclusions

A new helical phase (H*) from the self-assembly of PS-PLLA BCPs* was identified. The H* phase consists of hexagonally packed, interdigitated PLLA helical microdomains in a PS matrix; the space group of the phase was determined to be *P*622. A phase diagram of the BCP* was developed to establish the region in term of composition and molecular weight, over which

(35) Matsen, M. W. *J. Chem. Phys.* **1996**, *104*, 7758–7764.
(36) Joziasse, C. A. P.; Veenstra, H.; Grijpma, D. W.; Pennings, A. J. *Macromol. Chem. Phys.* **1996**, *197*, 2219–2229.
(37) Anderson, K. S.; Hillmyer, M. A. *Macromolecules* **2004**, *37*, 1857–1862.
(38) Grosberg, A. Y.; Khokhlov, A. R. *Statistical Physics of Macromolecules*; AIP: New York, 1994; pp 289−336.
(39) Ou-Yang, Z.-C.; Liu, J. *Phys. Rev. Lett.* **1990**, *65*, 1679–1682.
(40) Nandi, N.; Bagchi, B. *J. Am. Chem. Soc.* **1996**, *118*, 11208–11216.

the H* phase exists. Also, phase transitions from the H* phase to both the HC phase and G phase were found after long-time annealing, suggesting that the H* phase is a long-lived metastable phase. The T_{ODT} values of the PS-PLLA BCPs* always exceed those of the racemic PS-PLA BCPs given equivalent molecular weights and similar composition, indicating that the segregation strength between PS and chiral PLLA blocks is higher than that between PS and racemic PLA blocks. The chiral effect on the molecular interaction is significant and enhances the incompatibility between PS and PLLA blocks in the PS-PLLA BCPs*. The twisting interface of the PS-PLLA BCP* is induced by the steric hindrance of the PS-PLLA BCP chains for microphase separation and is amplified by the incompatible PS block and the further organization of partially ordered microdomains due to chiral interaction so as to develop helical microdomains.

Acknowledgment. Authors thank Dr. L. Rong of National Synchrotron Light Source at Brookhaven National Laboratory (U.S.A.) and Dr. U.-S. Jeng of National Synchrotron Radiation Research Center (Taiwan) for their help in synchrotron SAXS experiments. We also thank Dr. S. Z. D. Cheng of Institute of Polymer Science of University of Akron (U.S.A.) for his helpful discussion. Authors thank the National Science Council of the Republic of China, Taiwan, for financially supporting this research.

Supporting Information Available: Synthetic methods, simulations of projected images, and other experimental details. This material is available free of charge via the Internet at http://pubs.acs.org.

JA9083804